



Highly sensitive ratiometric fluorescent fiber matrices for oxygen sensing with micrometer spatial resolution

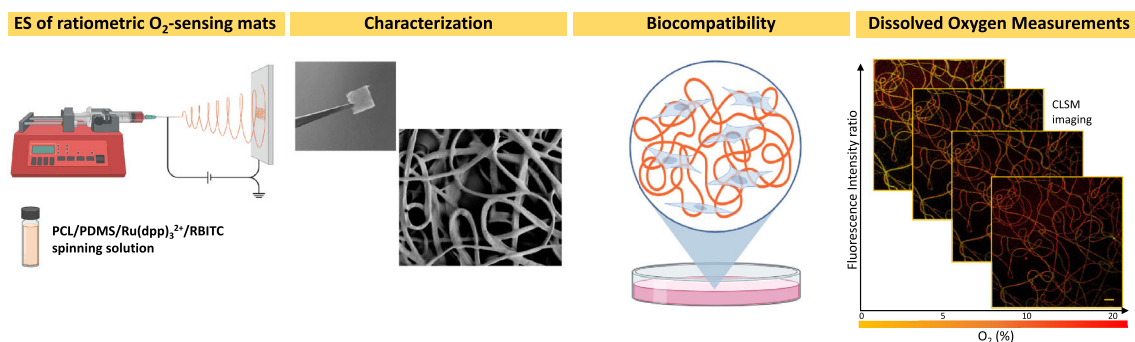
Giuliana Grasso¹ · Valentina Onesto¹ · Stefania Forciniti¹ · Eliana D'Amone¹ · Francesco Colella^{1,2} · Lara Pierantoni^{3,4} · Valeria Famà¹ · Giuseppe Gigli^{1,5} · Rui L. Reis^{3,4} · J. Miguel Oliveira^{3,4} · Loretta L. del Mercato¹

Received: 27 October 2023 / Accepted: 2 April 2024
© The Author(s) 2024

Abstract

Oxygen (O₂)-sensing matrices are promising tools for the live monitoring of extracellular O₂ consumption levels in long-term cell cultures. In this study, ratiometric O₂-sensing membranes were prepared by electrospinning, an easy, low-cost, scalable, and robust method for fabricating nanofibers. Poly(ϵ -caprolactone) and poly(dimethyl)siloxane polymers were blended with tris(4,7-diphenyl-1,10-phenanthroline) ruthenium(II) dichloride, which was used as the O₂-sensing probe, and rhodamine B isothiocyanate, which was used as the reference dye. The functionalized scaffolds were morphologically characterized by scanning electron microscopy, and their physicochemical profiles were obtained by Fourier transform infrared spectroscopy, thermogravimetric analysis, and water contact angle measurement. The sensing capabilities were investigated by confocal laser scanning microscopy, performing photobleaching, reversibility, and calibration curve studies toward different dissolved O₂ (DO) concentrations. Electrospun sensing nanofibers showed a high response to changes in DO concentrations in the physiological-pathological range from 0.5% to 20% and good stability under ratiometric imaging. In addition, the sensing systems were highly biocompatible for cell growth promoting adhesiveness and growth of three cancer cell lines, namely metastatic melanoma cell line SK-MEL2, breast cancer cell line MCF-7, and pancreatic ductal adenocarcinoma cell line Panc-1, thus recreating a suitable biological environment *in vitro*. These O₂-sensing biomaterials can potentially measure alterations in cell metabolism caused by changes in ambient O₂ content during drug testing/validation and tissue regeneration processes.

Graphic abstract



Keywords Electrospinning · Ruthenium(II) dichloride · Oxygen sensors · Ratiometric imaging · Fluorescence

Giuliana Grasso and Valentina Onesto have contributed equally to this work.

Extended author information available on the last page of the article

Published online: 29 April 2024

Introduction

Hypoxia, a condition in which a tissue gradually decreases in oxygen (O₂) levels, is generally recognized as a prodromic

event in cancer growth and progression. The master regulator driving hypoxia is hypoxia-inducible factor-1 [1], which is usually silent in normoxic conditions (5%–10% O₂) but strongly upregulated during anoxia (<1.5% O₂) in several cancer types, such as melanoma [2], breast cancer [3], and pancreatic ductal adenocarcinoma [4]. The pharmacological and clinical relevance of O₂ concentration makes it a well-recognized cancer biomarker [5].

Over the last few years, many strategies have been developed for sensing and imaging O₂ [6]. Optical O₂ sensors have become attractive because of various features such as reversibility, selectivity, and miniaturization. Moreover, optical sensors allow noninvasive measurements and image O₂ at high spatial resolutions (micrometer scale) [7, 8]. In recent years, many transition metal complexes (Ru²⁺, Os²⁺, and Ir³⁺) and metalloporphyrins (Pt²⁺ and Pd²⁺) have been used for producing optical O₂ sensors because of their capability to be dynamically quenched in the presence of dissolved O₂ (DO) [9]. Combining these O₂-sensing fluorescent probes with nonsensitive O₂ fluorophores, ratiometric optical systems that measure fluorescent signals at two different wavelengths can be produced. Ratiometric systems overcome some sensitivity limitations usually encountered in traditional optical sensors that measure fluorescence intensity only at a single wavelength (e.g., interference from analyte-independent factors, including instrumental parameters, local microenvironment, concentration of the probe, and photobleaching) [10–12]. Ratiometric O₂-sensing systems based on semiconducting quantum dots, nanoparticles and microparticles, and electrospun fibers prepared with natural [13] and synthetic [14] polymers have been successfully produced for monitoring intracellular O₂ concentration changes [15, 16]. For example, Xu et al. reported dual-emissive ratiometric nanoscale metal–organic frameworks (NMOFs) for intracellular quantification of O₂, showing that NMOFs were taken up by mouse colon carcinoma CT26 cells, allowing reliable measurements of cellular O₂ levels by confocal laser scanning microscopy (CLSM) [17]. In a different approach, Wen et al. reported a challenging protocol to engineer ratiometric afterglow/fluorescence dual-emissive O₂ polystyrene nanoparticles to explore the hypoxia environment in solid tumors when subcutaneously injected in mice bearing mouse sarcoma cell-derived S180 [18]. In addition, Gkika et al. designed poly-L-lysine-coated polystyrene particles encapsulating a new lipophilic and O₂-responsive ruthenium(II) (Ru(II)) tris-heteroleptic polypyridyl complex together with a reference BODIPY dye to sense normoxic and O₂-deprived (hypoxia) conditions after uptake in A549 lung carcinoma and HeLa cells [19]. Zhao et al. incorporated a highly efficient hydrophobic O₂ probe meso-5,10,15,20-tetrakis(pentafluorophenyl)porphyrinatoplatinum (PtTFPP) conjugated to a reference fluorescence resonance energy transfer donor inside the core of micelles to measure

O₂ concentration in HeLa cells [20]. Sensing extracellular changes of O₂ is fundamental because it is associated with extracellular matrix (ECM) remodeling and enhanced invadopodia and metastatic invasion [21, 22]. However, few examples have been reported in the literature regarding the production of diverse O₂ sensors based on the ratiometric approach to measure extracellular changes of O₂. For instance, Xue et al. demonstrated the extracellular detection of O₂ changes by producing electrospun core–shell poly(ε-caprolactone)/poly(dimethyl)siloxane (PCL/PDMS) nanofibers embedding O₂-quenching Ru complexes or platinum metalloporphyrin dyes in the PDMS core. Based on a single-wavelength detection approach, the fluorescent fiber matrices showed O₂-sensing properties and biocompatibility with glioma and glioma-derived primary cells [23].

In this study, an original protocol was proposed for the fabrication of PCL/PDMS nanofibers embedding an O₂-sensing tris(4,7-diphenyl-1,10-phenanthroline) Ru(II) dichloride (Ru(dpp)₃²⁺) probe and the O₂ nonsensitive dye rhodamine B isothiocyanate (RBITC) for the ratiometric sensing of microenvironmental changes of DO (Fig. 1). The homogenous blending of PDMS, PCL, Ru(dpp)₃²⁺, and RBITC was employed in the electrospinning technique, and fibers were obtained by a single ratiometric fluorescent polymeric solution, resulting in a low-cost and time-saving fabrication method compared to the previously reported core–shell setup [23, 24]. Moreover, the continuous ratiometric fluorescent polymer phase enabled the direct exposure of the O₂-sensing dye (Ru(dpp)₃²⁺) together with the O₂-permeable material (PDMS) not only within the lumen of the fiber but also at the interface with the surrounding environment, thus avoiding their confinement in the inner core of the fibers enclosed by an O₂ nonpermeable polymer shell. In addition, this study optimized ratiometric systems for sensing O₂, whose fluorescent signals are not affected by analyte-independent factors [12] usually encountered in fibrous platforms based on single-wavelength optical methods. Owing to their excellent cytocompatibility, these ratiometric O₂-sensing biomaterials are a promising platform for future applications in the live monitoring of O₂ consumption in biological environments and tissue engineering applications.

Materials and methods

Materials

RBITC (CAS no. 36877–69-7) mixed isomers and PCL (#440,744; M_{av} =80.000) were purchased from Sigma-Aldrich (Merck KGaA, Darmstadt, Germany). Sylgard® 184, a two-part silicone elastomer kit (PDMS), was purchased from Dow Corning Corp. (Midland, MI, USA). [Ru(dpp)₃²⁺]

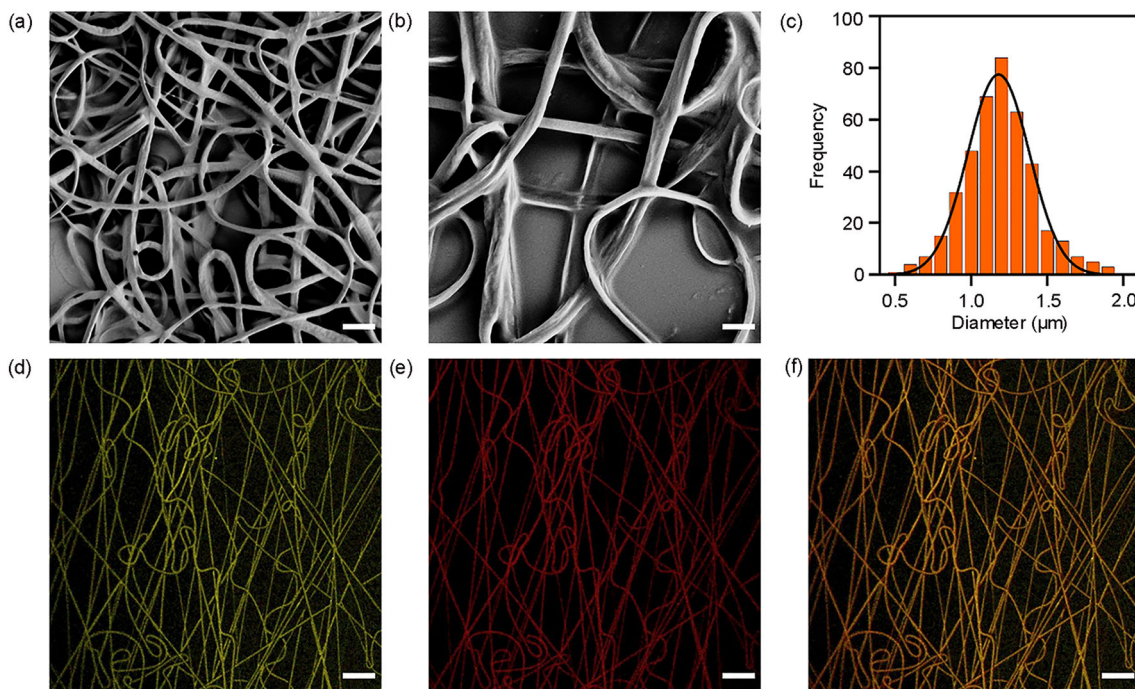


Fig. 1 Morphology of ratiometric O_2 -sensing fibers. **a, b** SEM micrographs of blended PCL/PDMS/Ru(dpp) $_3^{2+}$ /RBITC fibers at **a** $\times 2.5$ and **b** $\times 5$ magnifications. Scale bars: 10 μm (a) and 2 μm (b). **c** Size distribution studies. **d–f** Representative CLSM micrographs of PCL/PDMS/Ru(dpp) $_3^{2+}$ /RBITC fibers. The individual **d** yellow (false color; Ru(dpp) $_3^{2+}$: $\lambda_{\text{exc}}=405$ nm, $\lambda_{\text{em}}=550\text{--}650$ nm) and **e** red (RBITC: $\lambda_{\text{exc}}=561$ nm, $\lambda_{\text{em}}=570\text{--}620$ nm) channels are shown,

followed by **f** an overlay of the two channels (SP8, Leica, HC PL FLUOTAR $20\times/0.50$ dry objective, zoom 2.5; scale bar: 20 μm). SEM: scanning electron microscopy; PCL: poly(ϵ -caprolactone); PDMS: poly(dimethyl)siloxane; Ru(dpp) $_3^{2+}$: tris(4,7-phenyl-1,10-phenanthroline) ruthenium(II) dichloride; RBITC: rhodamine B isothiocyanate; CLSM: confocal laser scanning microscopy; λ_{exc} : excitation wavelength; λ_{em} : emission wavelength

2Cl^- (CAS no. 36309-88-3) were purchased from Alfa Aesar by Thermo Fisher Scientific (Haverhill, MA, USA). Methanol (MeOH; Reag. USP, Ph. Eur., for analysis, ACS, ISO; CAS no. 67-56-1), chloroform (CHCl_3 ; Reag. USP, Ph. Eur., for analysis, ACS, ISO; CAS no. 67-66-3), acetone (Reag. USP, Ph. Eur., for analysis, ACS, ISO; CAS no. 67-64-1), 2-propanol (IPA; Reag. USP, Ph. Eur., for analysis, ACS, ISO; CAS no. 67-63-0), and toluene (Reag. USP, Ph. Eur., for analysis, ACS, ISO; CAS no. 108-88-3) were purchased from PanReac AppliChem (Milan, Italy). *N,N*-dimethylformamide (DMF; anhydrous, 99.8%; CAS no. 68-12-2) was purchased from Sigma-Aldrich (Merck KGaA, Darmstadt, Germany). Tetrahydrofuran (THF; EMSURE[®] ACS, Reag. Ph. Eur., for analysis; CAS no. 109-99-9) was purchased from VWR Chemicals (Milan, Italy).

Fabrication of ratiometric O_2 -sensing fibers

For electrospinning of ratiometric O_2 -sensing fibers, PCL/PDMS blends containing dissolved Ru(dpp) $_3^{2+}$ and RBITC fluorophores were mixed in a solvent mixture and gently stirred in the dark at room temperature (RT) to obtain a homogeneous phase. PCL solutions (12% (0.12 g/mL))

were prepared 24 h in advance to allow for the full dissolution and homogenization of the polymer. To prepare PDMS, the elastomer and curing agent were weighed in a 10:1 ratio, mixed, and degassed in a vacuum pump for 20 min. The fluorophores Ru(dpp) $_3^{2+}$ and RBITC were prepared at a concentration of 1 mg/mL in each solvent system used in the study. Therefore, the electrospinning solution was composed of the following ratio: 1 part of PDMS (mass fraction) and 9 parts of 12% PCL, and a total amount of dyes representing the 0.10% (1 mg/mL) of the polymeric formulation. The solution was stirred (300 r/min) at RT for 2 h before electrospinning in the dark. For the electrospinning process, the solution was transferred into a 1 mL syringe (Henke Sass Wolf, Tuttlingen, Germany) equipped with a 21-gauge stainless steel blunt needle (Sterican[®], B-Braun, Milan, Italy). The syringe was placed on a syringe pump (E-fiber, SKE Research Equipment[®], Bollate, Italy), and the electrospun fibers were deposited directly onto the surface of square glasses (10 mm \times 10 mm) positioned on a stationary collector. The optimized parameters were as follows: flow rate, 0.8 mL/h; voltage, +14/−6 kV; tip–collector plate distance, 20 cm; time of deposition, 1 min. The environmental conditions were as follows: temperature range from 25 to 30 $^\circ\text{C}$ and relative humidity from 10% to 20%. The electrospun

fiber mat was finally exposed to the thermal polymerization process [25] by transferring the mat to a laboratory oven setup at 45 °C for 12 h. The samples were stored in the dark at RT in a vacuum desiccator until further use.

Characterization of ratiometric O₂-sensing fibers

The morphology of ratiometric O₂-sensing fibers was analyzed by scanning electron microscopy (SEM; Zeiss Sigma 500, Carl Zeiss, Germany). Before imaging, the fibers were sputtered-coated (compact coating unit CCU-010, SafeMatic GmbH, Zizers, Switzerland) with 10 nm gold (Target Au Ø 54 mm×0.2 mm; purity, 99.99%). Images were acquired using an accelerating voltage of 5 kV and a secondary electron detector (SE2) with magnifications of ×2500, ×5000, and ×10,000. The diameters of the fibers were then extracted by drawing linear regions of interest along the minor axis of the fibers in ImageJ (version 64-bit Java 1.8.0_172) [26]. Images of the most representative electrospun fibers are shown in Fig. S1 (Supplementary Information).

Thermogravimetric analysis (TGA) was carried out using a simultaneous thermal analyzer DSC/TGA STD Q600 (TA Instruments, Waters™, New Castel, DE, USA), and the samples were analyzed in an alumina pan after tare heating at 10 °C/min, from 25 to 800 °C, under N₂ atmosphere. Data were plotted and analyzed using the TA Universal Analysis 2000 version 4.5A (TA Instruments, Waters™, USA).

The chemical groups exposed on the fiber mat were observed using Fourier transform infrared (FTIR) spectroscopy via an FT/IR-6300 type A spectrophotometer (JASCO, Easton, MD, USA), set up in attenuated total reflectance ATR mode, with a resolution of 4 cm⁻¹, in the range from 500 to 4000 cm⁻¹. The samples were prepared by electrospun deposition on a piece of silicon wafer (previously washed in IPA and acetone and dried under a flux of N₂) and polymerized in a laboratory oven at 45 °C for 12 h before analysis.

The hydrophilicity of the fibers was calculated using a CAM 200 (KSV Instruments Ltd., Finland) instrument to measure the static water contact angles (WCAs; θ). For the experimental setup, the liquid (heavy phase) was represented by water (density: 0.9986 g/cm³), and the liquid (light phase) was air (density: 0.0013 g/cm³). The volume of the drop employed for the measurements and charged on the needle tip was 5 μ L. The WCA was calculated using Laplace-Young fitting, and data were the average of three measurements performed on different areas of each sample.

To functionalize the fibers, a Tergeo Plus plasma cleaner (PIE Scientific LLC, Union City, CA, USA) was used. The parameters adopted were 50% O₂ flow rate and 50% power for 0.3 min.

To measure the sensing performance of ratiometric O₂-sensing fibers to DO by CLSM imaging, the fiber samples

were placed in a four-well Ibidi® chamber plate, and 400 μ L of double distilled water (DDW) was added to each well. Calibrations were performed via CLSM (SP8 Leica Microsystems, Mannheim, Germany) in the O₂ concentration range of 0.5% to 20%, obtained by purging N₂ directly into DDW while measuring the O₂ content in water using a commercial O₂ meter (Vernier Go Direct® optical dissolved oxygen probe, Vernier Science Education, Beaverton, OR, USA), and about 30 min time was set to ensure that equilibrium was reached before measurement. Images were acquired using an HC PL FLUOTAR 20×/0.50 dry objective and 2.5 zoom (232.5 μ m×232.5 μ m). The emission wavelength (λ_{em}) of Ru(dpp)₃²⁺ and RBITC dyes was sequentially collected at λ_{em} =550–650 nm (excitation wavelength λ_{exc} =405 nm) and λ_{em} =570–620 nm (excitation wavelength λ_{exc} =561 nm), respectively. The CLSM images were processed with a custom algorithm written in GNU Octave (version 6.2.0) [27–29], opportunely modified to automatically quantify the fiber fluorescence intensities for ratiometric analyses. Briefly, the RBITC channel images were first converted to grayscale and binarized. Then, morphological opening with a disk-shaped element was performed to remove any small white noises in the image, and morphological closing was performed to remove any small holes in the object. In this way, the fibers were identified in the binarized reference channel image, which was used as a mask to store pixel locations and the corresponding fluorescence intensities $I_{Ru(dpp)_3^{2+}}/I_{RBITC}$ (obtained as the pixel-by-pixel ratio between fluorescence intensities of the original Ru(dpp)₃²⁺ and RBITC images, respectively). The mean and standard deviation from four different images were finally extracted.

Ratiometric measurements

To develop the sensing fibrous scaffold, Ru(dpp)₃²⁺ and RBITC were employed as an O₂-sensing reporter and non-sensitive O₂ dye, respectively, for ratiometric analyses. Whereas RBITC does not respond to O₂ concentration changes [30], the O₂ quenching mechanism of Ru complexes has been extensively reported in the literature [31, 32]. The linear dependence of the emission intensity behavior of Ru(dpp)₃²⁺ on the quencher concentration is governed by the Stern–Volmer equation (Eq. (1)) [33], reported as follows:

$$\frac{I_0}{I} = 1 + K_{sv}[O_2], \quad (1)$$

where I_0 and I are the fluorescence intensities in the absence and presence of the quencher, respectively; K_{sv} is the Stern–Volmer quenching constant; $[O_2]$ is the gaseous or dissolved oxygen concentration. In ideal conditions, the Stern–Volmer equation, plotted with the fluorescence intensities against O₂ concentrations, leads to a linear correlation

with a slope equal to K_{sv} and an intercept equal to 1, also providing information on the sensitivity of the sensor in relationship to O_2 quenching effect. In the ratiometric O_2 -sensing fiber system in this study, the fluorescent response of the $Ru(dpp)_3^{2+}$ complex and RBITC toward different O_2 concentrations is derived from the ratio (R) of the maximum fluorescence intensity of $Ru(dpp)_3^{2+}$ metal complex ($I_{[Ru(dpp)_3^{2+}]}$) to the maximum fluorescence intensity of O_2 -insensitive RBITC dye (I_{RBITC}), as follows:

$$R = \frac{I_{[Ru(dpp)_3^{2+}]}}{I_{RBITC}} \quad (2)$$

The Stern–Volmer equation is transformed by substituting I_0/I with R_0/R , representing the response of the ratiometric sensor, as follows:

$$\frac{R_0}{R} = 1 + K_{sv}[O_2], \quad (3)$$

where R_0 is the fluorescent signal in the absence of the quencher. Thus, it was possible to evaluate the ratiometric calibration curve of the developed sensing system.

Biocompatibility of ratiometric O_2 -sensing fibers

The biocompatibility of ratiometric O_2 -sensing scaffolds was evaluated by in vitro cytotoxicity assays using the melanoma cell line SK-MEL2 (HTB-68TM; ATCC, Rockville, MD, USA), human pancreatic cancer cell line Panc-1 (CRL-1469TM; ATCC, Rockville, USA), and breast cancer cell line MCF-7 (HTB-22TM; ATCC, Rockville, USA) cultured at 37 °C in a humidified 5% CO_2 incubator. SK-MEL2 cells were routinely cultured in Eagle's minimum essential medium (Sigma-Merck KGaA, Darmstadt, Germany), whereas Panc-1 and MCF-7 cells were grown in Dulbecco's modified Eagle's medium (Sigma-Merck KGaA, Darmstadt, Germany), both supplemented with 10% fetal bovine serum (Gibco, Thermo Fisher Scientific Inc., Waltham, MA, USA), 2 mmol L-glutamine, and 100 U/mL penicillin and streptomycin (Sigma-Merck KGaA, Darmstadt, Germany). Before cell culture experiments, O_2 -sensing fibers, deposited on 1 cm × 1 cm glass slides, were transferred to 24-well plates, sterilized by ultraviolet exposure for 30 min, and functionalized with 0.1 mg/mL fibronectin (Sigma-Merck KGaA, Darmstadt, Germany) for 30 min. Cells (4×10^4 per well) were seeded in each well, and their viability was evaluated using PrestoBlue cell viability reagent (Thermo Fisher Scientific Inc., Waltham, MA, USA) on Days 1, 3, and 6. Briefly, at each time point, 5 μ L PrestoBlue reagent was added to each well and incubated for 1 h at 37 °C and 5% CO_2 . The fluorescent signal was obtained using a microplate

reader (ClarioStarPlus, BMG Labtech, Germany) at an excitation wavelength of 535 nm and an emission wavelength of 590 nm. Cells grown directly in the well plate were used as controls.

Statistical analyses

All experiments were performed in triplicate, and the results were reported as the mean ± standard error unless otherwise stated. Statistical differences were considered significant at $p < 0.05$ using two-way analysis of variance. Data analyses and graphing were performed using Microsoft Excel 365 and GraphPad Prism (version 8.4.2-2018).

Results and discussion

Ratiometric O_2 -sensing fiber preparation and morphological observations

The fabrication of O_2 -sensing fibers was successfully assessed by coupling the advantages deriving from two polymers, namely PDMS and PCL. PDMS shows a high O_2 permeability coefficient ($P = 6.95 \times 10^{15} \text{ cm}^3$) resulting from the product of the diffusion constant and O_2 solubility coefficient [34]. However, PDMS lacks electrospinnability properties [35]. For this reason, PCL addition in the polymeric solution preparation was evaluated to allow the electrospinning of monolithic hybrid fibers. Notably, two fundamental aspects influenced the electrospinning of the hybrid polymeric matrix, particularly the swelling of PDMS in the solvent and the phenomenon of the partition of the solutes between the solvent and PDMS matrix [36]. Focusing on the PDMS swelling, using high-solubility solvents alone (e.g., chloroform and toluene), it is generally not compatible with the fabrication of PDMS-based devices because it causes marked swelling of the polymer. For this reason, it is usually recommended to prepare PDMS using a high-solubility solvent mixed with another low-solubility solvent (moderately to highly polar, e.g., water, alcohols, amides, and sulfoxides) to produce a mixture that does not swell PDMS or that at least reduces the swelling related to the use of high-solubility solvents. As anticipated, the other aspect considered during the preparation of the polymer matrix is the partitioning of the fluorophores ($Ru(dpp)_3^{2+}$ and RBITC) in the PDMS phase. This represents a key point for the preparation of O_2 -sensitive devices. Therefore, to prepare a homogeneous mixture of the solutes in the composite matrix composed of PCL and PDMS, it is necessary to use a low-solubility solvent capable of solvating both fluorophores, which neither reacts with the fluorophores nor quenches their fluorescence and, at the same time, does not cause crosslinking of the PDMS-PCL prepolymer blend [36].

Table 1 Details of the polymeric solution preparation to assess the electrospinning process and fiber fabrication

Sample codes	Solvent mixture	Polymer concentrations (%) and polymer ratio (pr)	Polymerization temperature (°C)	Morphology
F1A	DMF/THF (1:1)	PCL 12%	45	Fibers
F1B	DMF/THF (1:1)	PCL 12%	RT	Fibers
F2A	MeOH/CHCl ₃ (1:1)	PCL 12%	45	Fibers
F2B	MeOH/CHCl ₃ (1:1)	PCL 12%	RT	Fibers
F3A	DMF/THF (1:1)	PCL 12% + PDMS (pr 5:5)	45	Film forming
F3B	DMF/THF (1:1)	PCL 12% + PDMS (pr 5:5)	RT	Film forming
F4A	MeOH/CHCl ₃ (1:1)	PCL 12% + PDMS (pr 5:5)	45	Film forming
F4B	MeOH/CHCl ₃ (1:1)	PCL 12% + PDMS (pr 5:5)	RT	Film forming
F5A	DMF/THF (1:1)	PCL 12% + PDMS (pr 6:4)	45	Film forming
F5B	DMF/THF (1:1)	PCL 12% + PDMS (pr 6:4)	RT	Film forming
F6A	MeOH/CHCl ₃ (1:1)	PCL 12% + PDMS (pr 6:4)	45	Film forming
F6B	MeOH/CHCl ₃ (1:1)	PCL 12% + PDMS (pr 6:4)	RT	Film forming
F7A	DMF/THF (1:1)	PCL 12% + PDMS (pr 7:3)	45	Fibers
F7B	DMF/THF (1:1)	PCL 12% + PDMS (pr 7:3)	RT	Fibers
F8A	MeOH/CHCl ₃ (1:1)	PCL 12% + PDMS Sylgard® (pr 7:3)	45	Film forming
F8B	MeOH/CHCl ₃ (1:1)	PCL 12% + PDMS Sylgard® (pr 7:3)	RT	Film forming
F9A	DMF/THF (1:1)	PCL 12% + PDMS (PDMS dil 7:3)	45	Fibers
F9B	DMF/THF (1:1)	PCL 12% + PDMS (PDMS dil 7:3)	RT	Fibers
F10A	MeOH/CHCl ₃ (1:1)	PCL 12% + PDMS (PDMS dil 7:3)	45	Fibers
F10B	MeOH/CHCl ₃ (1:1)	PCL 12% + PDMS (PDMS dil 7:3)	RT	Film forming
F11A	CHCl ₃ /toluene (1:1)	PCL 12% + PDMS (PDMS dil 7:3)	45	Electrospray
F11B	CHCl ₃ /toluene (1:1)	PCL 12% + PDMS (PDMS dil 7:3)	RT	Electrospray
F12A	DMF/THF (1:1)	PCL 12% + PDMS (PDMS dil 8:2)	45	Film forming
F12B	DMF/THF (1:1)	PCL 12% + PDMS (PDMS dil 8:2)	RT	Film forming
F13A	MeOH/CHCl ₃ (1:1)	PCL 12% + PDMS (PDMS dil 8:2)	45	Film forming
F13B	MeOH/CHCl ₃ (1:1)	PCL 12% + PDMS (PDMS dil 8:2)	RT	Film forming
F14A	CHCl ₃ /toluene (1:1)	PCL 12% + PDMS (PDMS dil 8:2)	45	Electrospray
F14B	CHCl ₃ /toluene (1:1)	PCL 12% + PDMS (PDMS dil 8:2)	RT	Electrospray
F15	DMF/THF (1:1)	PCL 12% + PDMS (pr 9:1) + dyes	45	–
F16	MeOH/CHCl ₃ (1:1)	PCL 12% + PDMS (pr 9:1) + dyes	45	Fibers
F17	CHCl ₃ /toluene (1:1)	PCL 12% + PDMS (pr 9:1) + dyes	45	Electrospray

Morphology based on SEM analysis. All figures and size distribution studies of the electrospun samples are reported in Fig. S1 (Supplementary Information). SEM: scanning electron microscopy; DMF: N,N-dimethylformamide; THF: tetrahydrofuran; MeOH: methanol; CHCl₃: chloroform; PCL: poly(ϵ -caprolactone); PDMS: poly(dimethyl)siloxane; RT: room temperature; dil: dilution

Considering this knowledge, the experimental plan regarding the manufacturing of O₂-sensing fibers involved the preparation of a polymeric blend based on PCL and PDMS in different couples of solvent systems (namely, DMF/THF, CHCl₃/toluene, and MeOH/CHCl₃) to identify the best combination in terms of uniformity of the solution and good processability (Table 1).

The first step of this study involved the optimization of the electrospinning settings, including the voltage (+14/−6 kV), flow rate (0.8 mL/h), the distance between the needle tip and static collector (20 cm), and atmospheric temperature ($T=25\text{--}30\text{ }^{\circ}\text{C}$) and relative humidity (RH=30%–40%).

Another important optimized parameter was the polymerization temperature of the composite matrix [37] that had to consider the necessity of (i) not overcoming the low melting point of PCL, (ii) being optimal to crosslink the blend, and (iii) starting and lasting in a range of time that allows preserving the fiber shape. For these reasons, both RT and 45 °C, and 12 h as crosslinking time were chosen as study conditions. PCL, prepared for this work at the concentration of 12% (0.12 g/mL), was easily electrospun, resulting in defect-free and quite homogeneous fibers, in DMF/THF and MeOH/CHCl₃, although fibers left drying at RT were plain (Fig. S1, **F1B** and **F2B** in Supplementary Information)

compared to those dried in the oven at 45 °C (Fig. S1, **F1A** and **F2A** in Supplementary Information). Then, a study on the polymer ratio was conducted. The polymer blend in the solution system CHCl₃/toluene was not electrospun because a phase separation was obtained between the two polymers PCL and PDMS.

An equivalent amount of PCL and PDMS, at polymer ratio 5:5, determined the emulsion solution and the formation of foaming fibers (Fig. S1, **F3A**, **F3B**, **F4A**, and **F4B** in Supplementary Information). Similarly, the polymer ratio 6:4 (Table 1, F5A, F5B, F6A, and F6B) could not be electrospun at all, ascribed to the incompatibility of a high PDMS concentration, namely more than 30% of the total polymer blend weight percentage, in the electrospinning technique. The increase in PCL and decrease in PDMS in the polymer blend (7:3) formed straight fibers in DMF/THF solvent system (Fig. S1, **F7A** and **F7B** in Supplementary Information), whereas a wet glaze was observed around the central core of the fibers deriving from MeOH/CHCl₃ blend (Fig. S1, **F8A** and **F8B** in Supplementary Information). To enhance the electrospinnability and morphology of the fibers, PDMS was further diluted. In this step, the solution system CHCl₃/toluene was included in the study, considering the possibility of reducing the force at the interface of the polymer blend deriving from a diluted system. Therefore, the dilution of PDMS at the 7:3 ratio resulted in a heterogeneous population of fibers with different diameters in DMF/THF (Fig. S1, **F9A** and **F9B** in Supplementary Information) and unimodal fibers in MeOH/CHCl₃ with 5 μm diameter (Fig. S1, **F10A** and **F10B** in Supplementary Information), with a more rounded shape when polymerization occurred at 45 °C. In contrast, more diluted PDMS, at the ratio of 8:2, in the final polymer blend resulted in wet fibers with film foaming in both solvent systems of DMF/THF (Fig. S1, **F12A** and **F12B** in Supplementary Information) and MeOH/CHCl₃ (Fig. S1, **F13A** and **F13B** in Supplementary Information), due to the non-rapid evaporation of the solvents after fiber deposition. In contrast, the polymer blend in CHCl₃/toluene determined an electro spray phenomenon in the Taylor cone, again with no possibility of obtaining electrospun fibers (Table 1, F11A, F11B, F14A, and F14B) in 7:3 and 8:2 PDMS dilutions. The reason for this can be ascribed to the swelling effect of the couple of solvents CHCl₃/toluene on PDMS [36]. Considering the film forming fibers derived from an excess of solvent and its non-fast evaporation process at both RT and 45 °C, as last chance three polymer blends were prepared using PCL/PDMS (polymer ratio 9:1) with the addition of the dyes: (i) a polymer blend in MeOH/CHCl₃, resulting in a homogeneous phase (Table 1, F16); (ii) a polymer blend in CHCl₃/toluene, obtaining a phase separation (after vortexing and removal of the supernatant, electro spray phenomenon did not allow fiber fabrication) (Table 1, F17);

and (iii) a polymer blend in DMF/THF, which gave fluorophore quenching (for this reason, it was excluded from this study) (Table 1, F15). Considering the aim of validating a simple composite matrix and a feasible electrospinning method to prepare ratiometric O₂-sensing fibers, the polymer blend represented by the MeOH/CHCl₃ solvent system was selected.

Once the polymer ratio and electrospinning parameters were optimized, the influence of dye loading on the electrospinnability of the polymeric solution and the morphology of the resulting fibers were tested, together with their sensing performances. With this aim, comparative studies on the fabricated scaffolds were conducted to find the best concentration of each fluorescent component to obtain a final ratiometric system that guaranteed the successful entrapment of the luminescent probes within the fibers. Ru(dpp)₃²⁺ and RBITC stock solutions were prepared at 1 mg/mL concentration in MeOH/CHCl₃ (1:1) and used for the following study. Three concentrations of the reference dye RBITC and three concentrations of fluorophore Ru(dpp)₃²⁺ were charged in the composite polymer blend (Table S1 in Supplementary Information), and the effect of the probe cargo was detected via CLSM imaging. As expected, dye loading influenced the production protocol and the morphology of the scaffolds. Indeed, although the optimized fabrication parameters were applied to all solutions, the electrospinnability resulted in perturbation with the appearance of the electro spray phenomenon and current instabilities when conditions RS1, RS2, RS4, and RS6 (Table S1 in Supplementary Information) were adopted. In Fig. S2 (Supplementary Information), keeping the concentration of the sensing Ru-based complex constant (22 μg/mL), the increase in the cargo of the reference dye RBITC (conditions RS1 and RS2, Table S1 in Supplementary Information) determined a change in the pattern of the fibrous scaffold, which appeared nonhomogeneous in size and shape (Figs. S2a and S2b in Supplementary Information). Moreover, the fluorescent signals of RBITC appeared confined at the border of the electrospun strings, which instead presented a Ru(dpp)₃²⁺-rich core (Fig. S2b in Supplementary Information). In addition, the fibers appeared wet and oily, likely due to a slowing down or interruption of the curing process of the two PDMS components (elastomer and curing agent) within the polymeric mixture. These results agreed with those of a previous report [23] and did not allow the performing of any DO sensing test on the fabricated scaffolds. Thus, lowering the amount of the reference probe from 375 to 75 μg/mL (condition **RS3**, Table S1 in Supplementary Information) resulted in the colocalization of the ratiometric fluorescent signals that uniformly illuminated the entire fiber mat (Fig. S2c in Supplementary Information) upon laser excitation. Having established the RBITC cargo (75 μg/mL), Ru(dpp)₃²⁺ concentrations were also varied in the polymer solution to identify the optimal indicator loading amount for

ratiometric measurements. At this point, morphology and DO sensing ability were thoroughly investigated through confocal imaging analysis. An at least twofold increase in $\text{Ru}(\text{dpp})_3^{2+}$ to 90 or 360 $\mu\text{g}/\text{mL}$ (conditions **RS4** and **RS6**, Table S1 in Supplementary Information) caused difficulties in the application of the optimized electrospinning parameters, resulting in fibers losing their form and size in both cases (Figs. S3a and S3c in Supplementary Information), as observed previously. In addition, in the highest $\text{Ru}(\text{dpp})_3^{2+}$ concentration case (condition **RS6**, Table S1 in Supplementary Information), some fluorescent polymeric clusters in the blended electrospun fibers indicated an excessive amount of dye, resulting in molecular aggregation (Fig. S3c in Supplementary Information). Therefore, an intermediate amount of 180 $\mu\text{g}/\text{mL}$ of the Ru-based complex (condition **RS5**, Table S1 in Supplementary Information) within the polymer blend yielded bead-free, fluorescent, and microscaled scaffolds (Fig. S3b in Supplementary Information). The results from sensor sensitivity experiments at different DO concentrations are shown in Fig. S3d (Supplementary Information). Fluorescent emission responses were collected under the same excitation conditions and analyzed via image segmentation. For all sensing systems, intensity ratios in conditions **RS4**, **RS5**, and **RS6** were linearly correlated with the DO concentrations in the surrounding environment with similar slopes and regression coefficients. These results agreed with the expectations because although the amount of the sensing dye within the polymer solutions varied, the final scaffolds maintained the same sensing ability, being ratiometric platforms [12, 38, 39]. Clearly, the calibration curves reported higher intensity ratios when the amount of the Ru-based probe was increased while keeping the RBITC concentration constant. Although the intensity ratio ($I_{\text{Ru}(\text{dpp})_3^{2+}}/I_{\text{RBITC}}$) was maximized in correspondence with an excessive cargo of the fluorophores ($\geq 0.10\%$ (mass fraction) of the polymer blend), the sensing capacity was slightly reduced. Indeed, a diminished slope of the calibration curve of condition **RS6**, compared to **RS4** and **RS5** scaffolds, was obtained (Fig. S3d in Supplementary Information). Moreover, the high standard error during pixel-by-pixel analysis was a consequence of the nonhomogeneous distribution of the fluorescent probes within the fibers. Therefore, the fabrication condition **RS5**, with dyes representing 0.10% (mass fraction) of the polymeric formulation, was selected as the optimal balance to obtain a ratiometric optical sensing fibrous mat.

The microfiber morphology, investigated through SEM, revealed randomly oriented fibers with a continuous, smooth-surface, and bead-free structure with a string-like shape. Size distribution analyses evidenced uniform fiber diameters, with an average value of $(1.18 \pm 0.20) \mu\text{m}$ (Figs. 1a–1c). The uniform distribution of both fluorophores within the lumen of the

fibers, as visualized using CLSM, confirmed the promising ratiometric sensing platform (Figs. 1d–1f).

Ratiometric O_2 -sensing fiber structural characterization

The surface chemistry of the composite fibers was studied by FTIR in the ATR mode. The spectrum of blended PCL/PDMS fibers was compared with the spectra of PCL fibers and crosslinked PDMS solution because no fibers could be obtained from PDMS (Fig. 2a). From the FTIR spectrum of the blended fibers, it was possible to identify the typical bands of PCL, such as the carbonyl (C=O) overtone at 3446 cm^{-1} , the symmetric CH_2 stretching at 2938 and 2860 cm^{-1} , the carbonyl (C=O) stretching at 1725 cm^{-1} together with C–O and C–C stretching, the asymmetric C–O–C stretching at 1290 cm^{-1} , and O–C–O stretching at 1185 cm^{-1} [40, 41]. The proof of the blending solution came from the several characteristic bands of PDMS, such as the $-\text{CH}_3$ deformation in Si– CH_3 at 1260 cm^{-1} , the C–H bending corresponding to the peaks between 1400 and 1420 cm^{-1} , the Si–O–Si stretching at 1100 – 1000 cm^{-1} , and the Si–C rocking in the fingerprint region between 825 and 865 cm^{-1} [37, 42]. At 700 – 500 cm^{-1} , it was possible to find C–H stretching bands of adjacent aromatic and heterocyclic systems, typical of $\text{Ru}(\text{dpp})_3^{2+}$ and RBITC. All bands are reported in Table S2 (Supplementary Information).

The thermal properties of the polymer matrices were evaluated by TGA and differential scanning calorimetry (DSC) under a nitrogen atmosphere (Table 2). As established in the literature [43], the semicrystalline polymer PCL has a melting point (T_m) of about $60 \text{ }^\circ\text{C}$. In contrast, PDMS is a noncrystalline material and thus, has no melting point. However, the crosslinking process, occurring during the curing step of the microfibers at $45 \text{ }^\circ\text{C}$, determined a slight shift of the composite matrix glass transition to a higher temperature ($64.52 \text{ }^\circ\text{C}$), as shown in the DSC curve (Fig. S4 in Supplementary Information). Results in the TGA curves (Fig. 2b) demonstrated that from 350 to $450 \text{ }^\circ\text{C}$, PCL rapidly decomposed with complete weight loss (99.36%). In contrast, only 47.83% weight loss was observed for PDMS up to $800 \text{ }^\circ\text{C}$, indicating that PDMS had better thermal stability than PCL. Therefore, the preparation of composites based on these two polymers resulted in fiber matrices with higher thermal stability. Notably, the derivative thermogravimetric (DTG) curves confirmed the TGA results. The blend presented three degradation steps: the first decomposition peak was recorded at about 350 – $440 \text{ }^\circ\text{C}$, and this corresponded to PCL degradation; the second peak, at 440 – $500 \text{ }^\circ\text{C}$, was related to the fluorophores $\text{Ru}(\text{dpp})_3^{2+}$ and RBITC; and the third peak, at 530 – $630 \text{ }^\circ\text{C}$, was proper of PDMS breakdown of its crosslinked structure [44].

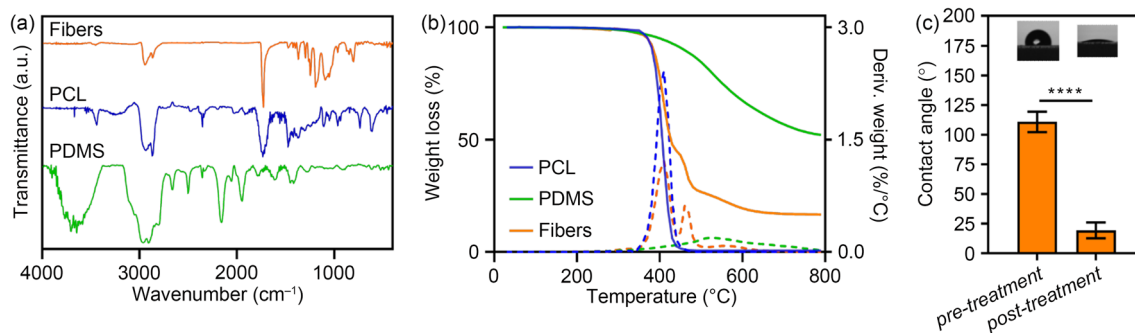


Fig. 2 Structural characterization of ratiometric O_2 -sensing fibers. **a** FTIR spectra of blended PCL/PDMS/Ru(dpp) $_3^{2+}$ /RBITC (orange line), PCL (blue line), and PDMS (green line). **b** TGA and DTG curves of PCL (straight and dot blue lines), PDMS (straight and dot green lines), and PCL/PDMS/Ru(dpp) $_3^{2+}$ /RBITC (straight and dot orange lines). **c** WCA analysis. Data are presented in mean \pm standard deviation

($n=3$), **** $p \leq 0.0001$. FTIR: Fourier transform infrared; PCL: poly(ϵ -caprolactone); PDMS: poly(dimethyl)siloxane; Ru(dpp) $_3^{2+}$: tris(4,7-diphenyl-1,10-phenanthroline) ruthenium(II) dichloride; RBITC: rhodamine B isothiocyanate; TGA: thermogravimetric analysis; DTG: derivative thermogravimetric analysis; WCA: water contact angle

Table 2 TGA of PCL, PDMS, and PCL/PDMS/Ru(dpp) $_3^{2+}$ /RBITC fibers

Sample	T_m ($^{\circ}C$)	T_i decomp. ($^{\circ}C$)	T_{max} decomp. ($^{\circ}C$)	Weight loss (%)	Residue (%)
PCL	61.59	350	410	99.36	0.64
PDMS	–	460	540	47.83	52.17
PCL/PDMS/Ru(dpp) $_3^{2+}$ /RBITC	64.52	360	570	83.20	16.80

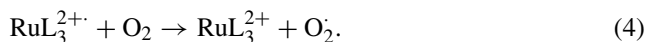
TGA: thermogravimetric analysis; PCL: poly(ϵ -caprolactone); PDMS: poly(dimethyl)siloxane; Ru(dpp) $_3^{2+}$: tris(4,7-diphenyl-1,10-phenanthroline) ruthenium(II) dichloride; RBITC: rhodamine B isothiocyanate; T_m : temperature of melting; T_i decomp.: initial decomposition temperature; T_{max} decomp.: maximum decomposition temperature

The overall performance of the developed scaffolds is dependent on the hydrophobicity of the fibrous mat, since this property can hinder the application of the sensing platform in vitro or in vivo [45, 46]. Therefore, the optimized ratiometric O_2 -sensing fibers were subjected to measuring the WCA using water as a liquid heavy phase (Fig. 2c). The drop of water deposited on the polymeric electrospun mats recorded a WCA $\theta \geq 110^{\circ} \pm 7^{\circ}$, indicating high hydrophobicity. To increase the wettability of the fibers, a functionalization step was performed with O_2 plasma (50% O_2 flow rate, 50% power, for 0.3 min), which increased the hydrophilicity of the surface due to the exposure of carboxylic and hydroxyl groups [45], endowing PCL/PDMS/Ru(dpp) $_3^{2+}$ /RBITC fibers with a WCA $\theta \leq 20^{\circ} \pm 6^{\circ}$.

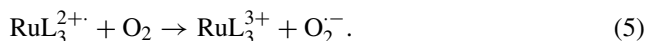
Ratiometric O_2 -sensing fibers: dose-response curve studies, photobleaching, and reversibility

One of the main aspects to consider during real-time DO concentration measurements in living systems is the sensitivity and stability of the analytical platform. As theoretically stated, the luminescence of Ru(II)-based polypyridyl complexes is governed by the metal–ligand charge transfer phenomenon. This latter process determines the transition of an electron from a metal d orbital to a ligand π^* orbital.

Consequently, upon excitation, the excited singlet state is converted to the lowest triplet state through intersystem crossing, generating the emissive fluorescence intensities of Ru polypyridyl complexes in a sensing system, which in turn is quenched by the presence of O_2 in the close environment [32]. In detail, two main reactions occur when O_2 interacts with Ru(dpp) $_3^{2+}$ complexes, thus quenching their fluorescence. Equation (4) describes the transition of an electron from Ru(dpp) $_3^{2+}$ complex (RuL) to give a single oxygen (O_2^{\cdot}) and the ground state of RuL, as shown below:



The second reaction involves the oxidation of the RuL operated by the transfer of an electron with subsequent production of the superoxide anion ($O_2^{\cdot -}$), as indicated below:



Therefore, when the 405 nm CLSM laser light excited the Ru(dpp) $_3^{2+}$ probe incorporated in the sensing scaffold, the absorption of light determined the energy gain of the excited electron, which, to restore its ground state, promoted energy release through fluorescence emission at higher wavelengths. Thus, the fluorescence behavior of Ru(dpp) $_3^{2+}$ was studied as a function of the DO concentration and resulted in the quenching phenomenon described

by the Stern–Volmer equation (see Section “Ratiometric measurements”). Although Ru complexes can sense DO concentrations alone, as reported previously [23], several factors during the analysis (e.g., operational, environmental, and instrumental variations) could interfere with and change the fluorescence read-out, resulting in inconsistent and inaccurate data. Herein, the fluorescence emission of RBITC upon excitation with the 561 nm CLSM laser light was not affected by the DO concentration. Therefore, the involvement of RBITC as a reference probe coupled to the Ru(dpp)_3^{2+} O_2 -sensing ability resulted in a ratiometric analytical method.

Here, the fluorescence response of ratiometric O_2 -sensing fibers was measured by recording the fluorescence of the fiber mats (1 cm × 1 cm glass squares) versus the DO concentrations from 0.5% to 20% (Fig. 3a). Figure 3a shows the fluorescence responses of Ru(dpp)_3^{2+} (yellow channel, false color) and RBITC (red channel) deriving from the DO concentration changes in the aqueous medium in which the fibers were immersed to perform the calibration by sequential CLSM acquisitions. The RBITC emission (red channel) was not subjected to any variations in terms of signal intensity. Meanwhile, the emission of Ru(dpp)_3^{2+} (yellow channel, false color) was strictly correlated with the local O_2 concentration, as expected from its photophysical behavior [31]. Indeed, in an almost hypoxic environment (0.5%), the Ru(dpp)_3^{2+} contained in the fibers emitted a remarkable and strong yellow signal (false color) when excited by 405 nm laser irradiation. Turning toward normoxic values (20%), the Ru(dpp)_3^{2+} signal visibly decreased in intensity, resulting in a clear observation of the RBITC emission (red channel) alone. An automated method was applied for the segmentation and analysis of CLSM images. Figure 3b shows the calibration curve extracted from the relation between fluorescence intensity ratios ($I_{\text{Ru(dpp)}_3^{2+}}/I_{\text{RBITC}}$) and DO levels. The linear fittings plotting the ratiometric calculation, with a correlation coefficient $R^2=0.9996$ (Fig. 3b), and the Stern–Volmer equation, with a correlation coefficient $R^2=0.9630$ (Fig. 3c), confirmed an efficient quenching phenomenon due to the sensing probe Ru(dpp)_3^{2+} in the presence of increasing O_2 concentrations in the sample. In contrast, RBITC showed a constant fluorescence intensity during the entire experiment, confirming its behavior as a reference fluorophore and therefore, its nonsensitivity to variations in O_2 concentration. To further highlight the performance of the developed scaffold, ratiometric O_2 -sensing fibers were tested for their stability under continuous illumination (photobleaching) by recording the changes in fluorescence emission intensities of Ru(dpp)_3^{2+} and RBITC

dyes as a function of time (Fig. 3d). The same area of the sample was illuminated for 10 min, recording one frame every minute. Photobleaching studies previously reported that the photobleaching rate for Ru complexes, in both solution and polymer matrices, could increase with time due to the production of reactive O_2 species, such as singlet molecular O_2 [47]. However, the PCL/PDMS/ Ru(dpp)_3^{2+} /RBITC fibers did not undergo a remarkable decay in the fluorescence intensity of the dyes under the tested experimental conditions, thus strengthening the advantages of the ratiometric sensing system. Finally, the reversibility of the fibers to switches in O_2 concentrations was monitored by applying four consecutive cycles of 0.5%–19.6% O_2 concentration switches. Even in this case, the ratiometric calculations were extrapolated after four switch cycles to obtain quantitative data regarding the reversibility test. In Fig. 3e, the ability of the sensing scaffold to rapidly change the read-out from a higher to a lower intensity confirmed the reversibility of the system and the potentiality of the matrix to monitor relevant DO levels in real time.

These results showed that hybrid monolithic electrospun fibers could efficiently disperse Ru(dpp)_3^{2+} /RBITC fluorophores, allowing for reliable, rapid, and stable ratiometric optical sensing and imaging of DO variations.

Biocompatibility of ratiometric O_2 -sensing fibers

The biocompatibility of ratiometric O_2 -sensing fibers was investigated using three cancer cell lines. To this aim, SK-MEL2, Panc-1, or MCF-7 cells were cultured on a two-dimensional (2D) adherent surface (control) and ratiometric O_2 -sensing fibers, and their viability was measured for up to six days using the PrestoBlue[®] assay. The CLSM images in Fig. 4 show all tested tumor cells adhered to PCL/PDMS/ Ru(dpp)_3^{2+} /RBITC fibers, retaining their typical epithelial morphology. Notably, cells on the fibrous matrices formed small groups that clustered together (arrows in Figs. 4a–4c). Cell proliferation was monitored after 1, 3, and 6 d of culture. In Fig. 4d, no cytotoxicity was observed regarding cell growth on the PCL/PDMS/ Ru(dpp)_3^{2+} /RBITC fibers compared to a 2D adherent surface. Interestingly, all tested cell lines cultured onto the fibrous scaffolds showed better growth than those observed for cultures on 2D adherent surfaces (Figs. 4d–4f). These results suggested that the obtained system can recreate a suitable biological microenvironment for tumor cell growth over time.

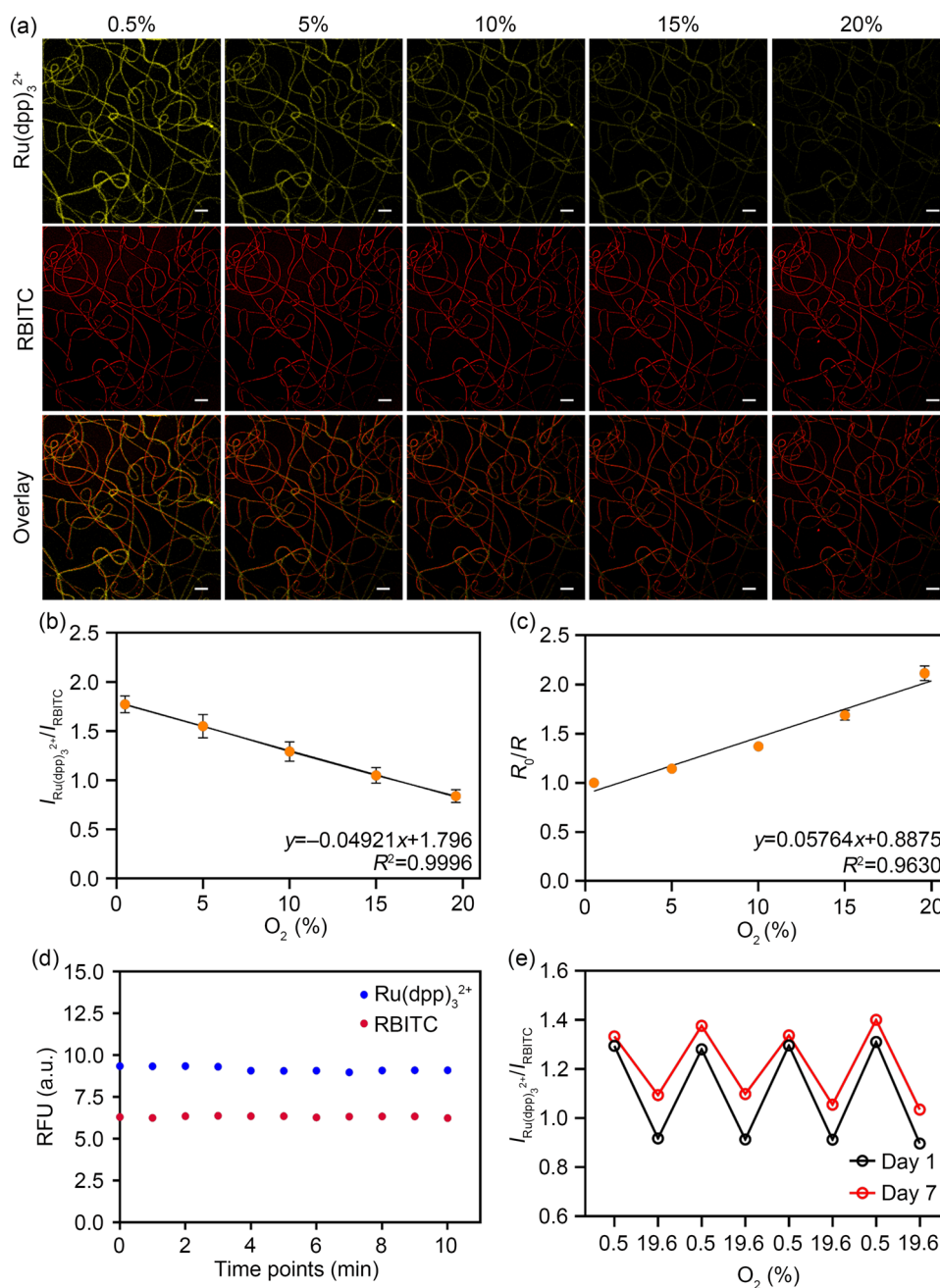


Fig. 3 CLSM imaging and sensing properties of ratiometric O₂-sensing fibers. **a** Representative CLSM micrographs showing the fluorescence response of PCL/PDMS/Ru(dpp)₃²⁺/RBITC fibers versus different DO levels (0.5%–20% concentration). The individual yellow (false color; Ru(dpp)₃²⁺: $\lambda_{\text{exc}}=405$ nm, $\lambda_{\text{em}}=550$ –650 nm) and red (RBITC: $\lambda_{\text{exc}}=561$ nm, $\lambda_{\text{em}}=570$ –620 nm) channels of CLSM images are shown, followed by an overlay of the two channels. Scale bar: 10 μm. **b** O₂-calibration curve of the sensing scaffolds as a function of O₂ concentration: the fluorescence intensity ratios between the O₂-sensitive dye Ru(dpp)₃²⁺ at 550–650 nm ($\lambda_{\text{exc}}=405$ nm) and the reference fluorophore RBITC at 570–620 nm ($\lambda_{\text{exc}}=561$ nm) were plotted versus the O₂ concentrations obtained by fluxing N₂ in DDW. The points reported in the plot are the means of three independent readings. Error bars show the standard deviations. **c** Stern–Volmer plot of the fibrous ratiometric optical sensing system: the fluorescence ratiometric behavior of Ru(dpp)₃²⁺ ($\lambda_{\text{exc}}=405$ nm; $\lambda_{\text{em}}=550$ –650 nm)

($\lambda_{\text{exc}}=561$ nm; $\lambda_{\text{em}}=570$ –620 nm) was plotted versus the O₂ concentrations, obtained by fluxing N₂ in DDW, to achieve the Stern–Volmer curve. **d** Photobleaching test: the fluorescence intensities of Ru(dpp)₃²⁺ and RBITC signals were recorded by CLSM in time-lapse mode, illuminating the sample for 10 min (1 frame/min). **e** Reversibility of O₂-sensing fibers evaluated by conducting sequences of four O₂ concentration switches between 0.5% and 19.6%. The aging of O₂-sensing PCL/PDMS fibers was evaluated by repeating sequences of four O₂ switches after 7 d on the samples adopted to evaluate the reversibility. CLSM: confocal laser scanning microscopy; PCL: poly(ϵ -caprolactone); PDMS: poly(dimethyl)siloxane; Ru(dpp)₃²⁺: tris(4,7-diphenyl-1,10-phenanthroline) ruthenium(II) dichloride; RBITC: rhodamine B isothiocyanate; DO: dissolved oxygen; λ_{exc} : excitation wavelength; λ_{em} : emission wavelength; DDW: double distilled water; RFU: relative fluorescence units

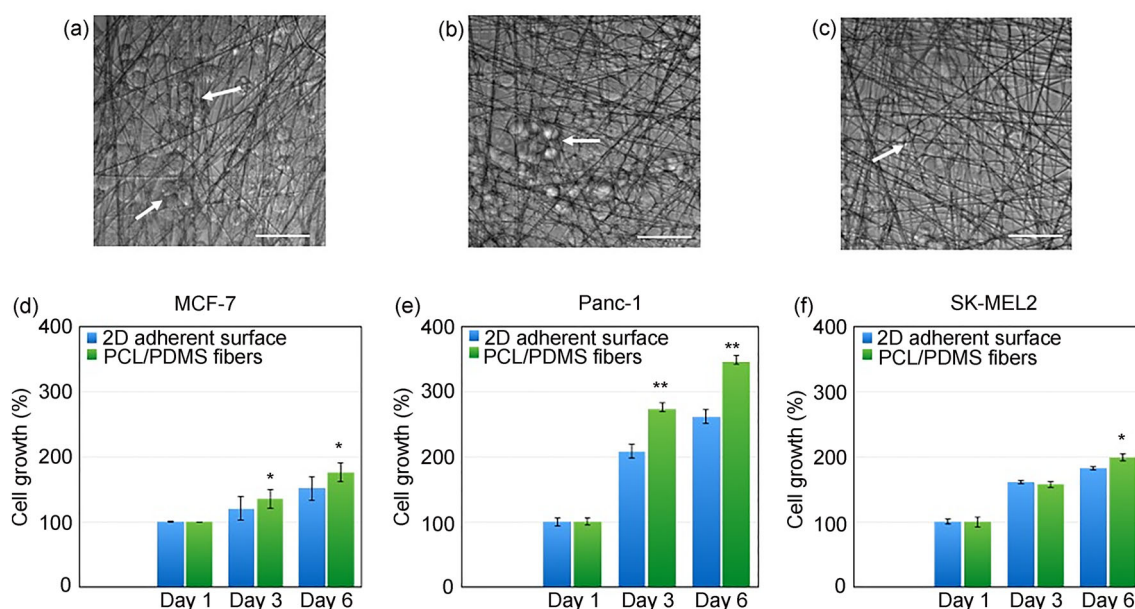


Fig. 4 Biocompatibility and cell proliferation on ratiometric O_2 -sensing fibers of **a, d** breast cancer cells (MCF-7), **b, e** human pancreatic cancer cells (Panc-1), and **c, f** malignant melanoma cells (SK-MEL2). Cell viability was measured using PrestoBlue[®] reagent as described in Section “Materials and methods”. Scale bar: 50 μ m. Data are presented

in mean \pm standard error of three independent experiments, * $p < 0.05$, ** $p < 0.01$, 2D adherent surface versus PCL/PDMS fibers for each time point. PCL: poly(ϵ -caprolactone); PDMS: poly(dimethyl)siloxane; 2D: two-dimensional

Conclusions

The O_2 indicator probe $Ru(dpp)_3^{2+}$ and the reference dye RBITC were coembedded within the lumen of monolithic PCL/PDMS fibers, yielding a hybrid platform for the imaging and ratiometric optical sensing of DO in a liquid medium. The system combines the properties of the carrier polymer PCL with the transparency and permeability of PDMS to O_2 and the simplicity of the setup configuration for spinning monolithic fibers. Physicochemical and morphological properties together with stability tests of PCL/PDMS/ $Ru(dpp)_3^{2+}$ /RBITC fibers were analyzed in detail, revealing the production of bead-free randomly oriented and ratiometric O_2 -sensing fibers characterized by a fast, highly reproducible, and stable response to DO over time. O_2 gradients emulating normoxic and hypoxic conditions were detected through three-dimensional confocal imaging of ratiometric PCL/PDMS/ $Ru(dpp)_3^{2+}$ /RBITC fibers. The emission ratio ($I_{Ru(dpp)_3^{2+}}/I_{RBITC}$) was strictly correlated with the local DO concentration, indicating a linear sensitivity in the 0.5%–20% range. Interestingly, when the response of the hybrid fibers was evaluated during drastic switches in O_2 concentrations, they expressed the ability to rapidly change their read-out, attesting to their reversibility and potential to detect DO levels in real time. These data supported the use of such a sensing platform for precisely and spatiotemporally monitoring O_2 extracellular changes and the metabolism of cells in in vitro or in vivo disease models, evaluating how O_2 changes promote or reduce the efficacy

of targeted therapies for tumor treatment. Additional sensors (e.g., pH or lactate probes) could be integrated into the lumen of the fiber, and their application for noninvasive and accurate in situ microenvironment investigation of target analytes could be exploited because of the high cytocompatibility of the ECM-like fiber mats.

Supplementary Information The online version contains supplementary material available at <https://doi.org/10.1007/s42242-024-00277-3>.

Acknowledgements The authors acknowledge funding from the European Research Council (ERC) under the European Union’s (EU’s) Horizon 2020 research and innovation program ERC Starting Grant “INTERCELLMED” (No. 759959), the EU’s Horizon 2020 research and innovation program under grant agreement No. 953121 (FLAMIN-GO), the Associazione Italiana per la Ricerca contro il Cancro (AIRC; MFAG-2019; No. 22902), the “Tecnopolo per la medicina di precisione” (TecnoMed Puglia)—Regione Puglia: DGR n.2117 of 21/11/2018, B84118000540002, the Italian Ministry of Research (MUR) in the framework of the National Recovery and Resilience Plan (NRRP), “NFFA-DI” Grant (n. B53C22004310006), “I-PHOQS” Grant (n. B53C22001750006) and under the complementary actions to the NRRP, “Fit4MedRob” Grant (PNC0000007, n. B53C22006960001), “ANTHEM” Grant (PNC0000003, n. B53C22006710001), funded by NextGenerationEU and the PRIN 2022 (2022CRFNCP_PE11_PRIN2022) funded by European Union—Next Generation EU. The authors also acknowledge the financial support provided under the project “HEALTH-UNORTE: Setting-up biobanks and regenerative medicine strategies to boost research in cardiovascular, musculoskeletal, neurological, oncological, immunological, and infectious diseases” (reference NORTE-01-0145-FEDER-000039) funded by the Norte Portugal Regional Coordination and Development Commission (CCDR-N) under the NORTE2020 Program. The authors thank Dr. Anil Chandra (Center for Research in Pure

and Applied Sciences, Bangalore, India) for the initial support and Dr. Alessandra Quarta (Institute of Nanotechnology, Lecce, Italy) for providing MCF-7 breast cancer cells. SF also acknowledges the AIRC Short-term Fellowship program.

Author contributions GG (Giuliana Grasso) was contributed to conceptualization, methodology, investigation, formal analysis, data curation, validation, writing—original draft, writing—review and editing; VO was contributed to methodology, investigation, formal analysis, data curation, software, validation, writing—review and editing; SF was contributed to methodology, investigation, formal analysis, data curation, validation, writing—review and editing; EDA, FC, LP, and VF were contributed to methodology, investigation, formal analysis, visualization; GG (Giuseppe Gigli) and RLR were contributed to resources, funding acquisition, project administration, visualization; JMO and LLDM were contributed to conceptualization, data curation, visualization, funding acquisition, resources, writing—review and editing, supervision.

Funding Open access funding provided by Consiglio Nazionale Delle Ricerche (CNR) within the CRUI-CARE Agreement.

Declarations

Conflict of interest This paper is to be included in a special issue for which RLR and JMO are guest editors. JMO is an editorial board member for *Bio-Design and Manufacturing*. They were not involved in the editorial review or the decision to publish this article. The authors declare that they have no conflict of interest.

Ethical approval This article does not contain any studies with human or animal subjects performed by any of the authors.

Open Access This article is licensed under a Creative Commons Attribution 4.0 International License, which permits use, sharing, adaptation, distribution and reproduction in any medium or format, as long as you give appropriate credit to the original author(s) and the source, provide a link to the Creative Commons licence, and indicate if changes were made. The images or other third party material in this article are included in the article's Creative Commons licence, unless indicated otherwise in a credit line to the material. If material is not included in the article's Creative Commons licence and your intended use is not permitted by statutory regulation or exceeds the permitted use, you will need to obtain permission directly from the copyright holder. To view a copy of this licence, visit <http://creativecommons.org/licenses/by/4.0/>.

References

1. Kim LC, Simon MC (2022) Hypoxia-inducible factors in cancer. *Cancer Res* 82(2):195–196. <https://doi.org/10.1158/0008-5472.CAN-21-3780>
2. D'Aguanno S, Mallone F, Marengo M et al (2021) Hypoxia-dependent drivers of melanoma progression. *J Exp Clin Cancer Res* 40(1):159. <https://doi.org/10.1186/s13046-021-01926-6>
3. Tang K, Zhu LY, Chen J et al (2021) Hypoxia promotes breast cancer cell growth by activating a glycogen metabolic program. *Cancer Res* 81(19):4949–4963. <https://doi.org/10.1158/0008-5472.CAN-21-0753>
4. Tao JX, Yang G, Zhou WC et al (2021) Targeting hypoxic tumor microenvironment in pancreatic cancer. *J Hematol Oncol* 14(1):14. <https://doi.org/10.1186/s13045-020-01030-w>
5. Sebestyén A, Kopper L, Dankó T et al (2021) Hypoxia signaling in cancer: from basics to clinical practice. *Pathol Oncol Res* 27:1609802. <https://doi.org/10.3389/pore.2021.1609802>
6. Roussakis E, Li ZX, Nichols AJ et al (2015) Oxygen-sensing methods in biomedicine from the macroscale to the microscale. *Angew Chemie Int Ed* 54(29):8340–8362. <https://doi.org/10.1002/anie.201410646>
7. Yoshihara T, Hirakawa Y, Hosaka M et al (2017) Oxygen imaging of living cells and tissues using luminescent molecular probes. *J Photochem Photobiol C Photochem Rev* 30:71–95. <https://doi.org/10.1016/j.jphotochemrev.2017.01.001>
8. Wang XD, Wolfbeis OS (2014) Optical methods for sensing and imaging oxygen: materials, spectroscopies and applications. *Chem Soc Rev* 43(10):3666–3761. <https://doi.org/10.1039/C4CS00039K>
9. Grist SM, Bennewith KL, Cheung KC (2022) Oxygen measurement in microdevices. *Annu Rev Anal Chem* 15(1):221–246. <https://doi.org/10.1146/annurev-anchem-061020-111458>
10. Raju LJ, Rajkumar E (2023) Coordination compounds of iron, ruthenium and osmium. In: Ameta R, Rai AK, Bhatt JP et al (Eds.), *Photochemistry and Photophysics of Coordination Compounds*. Elsevier, Amsterdam, p.135–203. <https://doi.org/10.1016/B978-0-12-824493-7.00008-3>
11. Gui RJ, Jin H, Bu XN et al (2019) Recent advances in dual-emission ratiometric fluorescence probes for chemo/biosensing and bioimaging of biomarkers. *Coord Chem Rev* 383:82–103. <https://doi.org/10.1016/j.ccr.2019.01.004>
12. Bigdeli A, Ghasemi F, Abbasi-Moayed S et al (2019) Ratiometric fluorescent nanoprobe for visual detection: design principles and recent advances—a review. *Anal Chim Acta* 1079:30–58. <https://doi.org/10.1016/j.aca.2019.06.035>

13. Feng Q, Zhang KY, Yang BG et al (2022) Editorial: biomedical applications of natural polymers. *Front Bioeng Biotechnol* 10:1077823. <https://doi.org/10.3389/fbioe.2022.1077823>
14. Wei Q, Deng NN, Guo JL et al (2018) Synthetic polymers for biomedical applications. *Int J Biomater* 2018:7158621. <https://doi.org/10.1155/2018/7158621>
15. Chandra A, Prasad S, Gigli G et al (2020) Fluorescent nanoparticles for sensing. In: Parak WJ, Feliu N (Eds.), *Colloids for Nanobiotechnology* (1st Ed.). Elsevier Ltd., Amsterdam, p.117–149. <https://doi.org/10.1016/B978-0-08-102828-5.00006-1>
16. Grasso G, Colella F, Forciniti S et al (2023) Fluorescent nano- and microparticles for sensing cellular microenvironment: past, present and future applications. *Nanoscale Adv* 5:4311–4336. <https://doi.org/10.1039/D3NA00218G>
17. Xu RY, Wang YF, Duan XP et al (2016) Nanoscale metal–organic frameworks for ratiometric oxygen sensing in live cells. *J Am Chem Soc* 138(7):2158–2161. <https://doi.org/10.1021/jacs.5b13458>
18. Wen Y, Zhang SD, Yuan W et al (2023) Afterglow/fluorescence dual-emissive ratiometric oxygen probe for tumor hypoxia imaging. *Anal Chem* 95(4):2478–2486. <https://doi.org/10.1021/acs.analchem.2c04764>
19. Gkika KS, Kargaard A, Burke CS et al (2021) Ru(II)/BODIPY core co-encapsulated ratiometric nanotools for intracellular O₂ sensing in live cancer cells. *RSC Chem Biol* 2(5):1520–1533. <https://doi.org/10.1039/D1CB00102G>
20. Zhao Q, Pan TT, Xiang G et al (2018) Highly efficient ratiometric extracellular oxygen sensors through physical incorporation of a conjugated polymer and PtTFPP in graft copolymers. *Sensor Actuat B Chem* 273:242–252. <https://doi.org/10.1016/j.snb.2018.06.026>
21. Murphy DA, Courtneidge SA (2011) The “ins” and “outs” of podosomes and invadopodia: characteristics, formation and function. *Nat Rev Mol Cell Biol* 12(7):413–426. <https://doi.org/10.1038/nrm3141>
22. Shin DS, Schroeder ME, Anseth KS (2022) Impact of collagen triple helix structure on melanoma cell invadopodia formation and matrix degradation upon BRAF inhibitor treatment. *Adv Healthc Mater* 11(7):e2101592. <https://doi.org/10.1002/adhm.202101592>
23. Xue RP, Behera P, Xu J et al (2014) Polydimethylsiloxane core–polycaprolactone shell nanofibers as biocompatible, real-time oxygen sensors. *Sensor Actuat B Chem* 192:697–707. <https://doi.org/10.1016/j.snb.2013.10.084>
24. Xue RP, Ge C, Richardson K et al (2015) Microscale sensing of oxygen via encapsulated porphyrin nanofibers: effect of indicator and polymer “core” permeability. *ACS Appl Mater Interfaces* 7(16):8606–8614. <https://doi.org/10.1021/acsami.5b00403>
25. Bardelli T, Marano C, Briatico Vangosa F (2021) Polydimethylsiloxane crosslinking kinetics: a systematic study on Sylgard184 comparing rheological and thermal approaches. *J Appl Polym Sci* 138(39):e51013. <https://doi.org/10.1002/app.51013>
26. Schneider CA, Rasband WS, Eliceiri KW (2012) NIH image to ImageJ: 25 years of image analysis. *Nat Methods* 9(7):671–675. <https://doi.org/10.1038/nmeth.2089>
27. Rizzo R, Onesto V, Forciniti S et al (2022) A pH-sensor scaffold for mapping spatiotemporal gradients in three-dimensional in vitro tumour models. *Biosens Bioelectron* 212:114401. <https://doi.org/10.1016/j.bios.2022.114401>
28. Onesto V, Forciniti S, Alemanno F et al (2023) Probing single-cell fermentation fluxes and exchange networks via pH-sensing hybrid nanofibers. *ACS Nano* 17(4):3313–3323. <https://doi.org/10.1021/acsnano.2c06114>
29. Rizzo R, Onesto V, Morello G et al (2023) pH-sensing hybrid hydrogels for non-invasive metabolism monitoring in tumor spheroids. *Mater Today Bio* 20:100655. <https://doi.org/10.1016/j.mtbio.2023.100655>
30. Zeng S, Liu XS, Kafuti YS et al (2023) Fluorescent dyes based on rhodamine derivatives for bioimaging and therapeutics: recent progress, challenges, and prospects. *Chem Soc Rev* 52(16):5607–5651. <https://doi.org/10.1039/d2cs00799a>
31. Demas JN, Diemente D, Harris EW (1973) Oxygen quenching of charge-transfer excited states of ruthenium(II) complexes. Evidence for singlet oxygen production. *J Am Chem Soc* 95(20):6864–6865. <https://doi.org/10.1021/ja00801a073>
32. Quaranta M, Borisov SM, Klimant I (2012) Indicators for optical oxygen sensors. *Bioanal Rev* 4(2–4):115–157. <https://doi.org/10.1007/s12566-012-0032-y>
33. Gehlen MH (2020) The centenary of the Stern–Volmer equation of fluorescence quenching: from the single line plot to the SV quenching map. *J Photochem Photobiol C Photochem Rev* 42:100338. <https://doi.org/10.1016/j.jphotochemrev.2019.100338>
34. Amao Y (2003) Probes and polymers for optical sensing of oxygen. *Microchim Acta* 143(1):1–12. <https://doi.org/10.1007/s00604-003-0037-x>
35. Yang DY, Liu X, Jin Y et al (2009) Electrospinning of poly(dimethylsiloxane)/poly(methyl methacrylate) nanofibrous membrane: fabrication and application in protein microarrays. *Biomacromolecules* 10(12):3335–3340. <https://doi.org/10.1021/bm900955p>
36. Lee JN, Park C, Whitesides GM (2003) Solvent compatibility of poly(dimethylsiloxane)-based microfluidic devices. *Anal Chem* 75(23):6544–6554. <https://doi.org/10.1021/ac0346712>
37. Berean K, Ou JZ, Nour M et al (2014) The effect of crosslinking temperature on the permeability of PDMS membranes: evidence of extraordinary CO₂ and CH₄ gas permeation. *Sep Purif Technol* 122:96–104. <https://doi.org/10.1016/j.seppur.2013.11.006>
38. Huang XL, Song JB, Yung BC et al (2018) Ratiometric optical nanoprobes enable accurate molecular detection and imaging. *Chem Soc Rev* 47(8):2873–2920. <https://doi.org/10.1039/C7CS00612H>
39. Pei XY, Pan Y, Zhang LC et al (2021) Recent advances in ratiometric luminescence sensors. *Appl Spectrosc Rev* 56(4):324–345. <https://doi.org/10.1080/05704928.2020.1793770>
40. Riaz U, Ashraf SM (2014) Characterization of polymer blends with FTIR spectroscopy. In: Thomas S, Grohens Y, Jyotishkumar P (Eds.), *Characterization of Polymer Blends*. Wiley, Hoboken, p.625–678. <https://doi.org/10.1002/9783527645602.ch20>
41. Fiore T, Pellerito C (2021) Infrared absorption spectroscopy. In: Simonpietro A (Ed.), *Spectroscopy for Materials Characterization*. Wiley, Hoboken, p 129–167. <https://doi.org/10.1002/9781119698029.ch5>
42. Gupta NS, Lee KS, Labouriau A (2021) Tuning thermal and mechanical properties of polydimethylsiloxane with carbon fibers. *Polymers* 13(7):1141. <https://doi.org/10.3390/polym13071141>

43. Guarino V, Gentile G, Sorrentino L et al (2017) Polycaprolactone: synthesis, properties, and applications. In: Mark HF (Ed.), *Encyclopedia of Polymer Science and Technology*. Wiley, Hoboken, p.1–36. <https://doi.org/10.1002/0471440264.pst658>
44. Wang Y, Cai YB, Zhang H et al (2021) Mechanical and thermal degradation behavior of high-performance PDMS elastomer based on epoxy/silicone hybrid network. *Polymer* 236:124299. <https://doi.org/10.1016/j.polymer.2021.124299>
45. Niemczyk-Soczynska B, Gradys A, Sajkiewicz P (2020) Hydrophilic surface functionalization of electrospun nanofibrous scaffolds in tissue engineering. *Polymers* 12(11):2636. <https://doi.org/10.3390/polym12112636>
46. Zupančič Š (2019) Core-shell nanofibers as drug delivery systems. *Acta Pharm* 69(2):131–153. <https://doi.org/10.2478/acph-2019-0014>
47. Fuller ZJ, Bare WD, Kneas KA et al (2003) Photostability of luminescent ruthenium(II) complexes in polymers and in solution. *Anal Chem* 75(11):2670–2677. <https://doi.org/10.1021/ac0261707>

Authors and Affiliations

Giuliana Grasso¹  · Valentina Onesto¹  · Stefania Forciniti¹  · Eliana D'Amone¹ · Francesco Colella^{1,2}  · Lara Pierantoni^{3,4}  · Valeria Famà¹ · Giuseppe Gigli^{1,5}  · Rui L. Reis^{3,4}  · J. Miguel Oliveira^{3,4}  · Loretta L. del Mercato¹ 

✉ J. Miguel Oliveira
miguel.oliveira@i3bs.uminho.pt

✉ Loretta L. del Mercato
loretta.delmercato@nanotec.cnr.it

¹ Institute of Nanotechnology, National Research Council (CNR-NANOTEC), c/o Campus Ecotekne, via Monteroni, 73100 Lecce, Italy

² Department of Mathematics and Physics “Ennio De Giorgi”, University of Salento, c/o Campus Ecotekne, via Monteroni, 73100 Lecce, Italy

³ 3B's Research Group, I3Bs–Research Institute on Biomaterials, Biodegradables and Biomimetics, Headquarters of the European Institute of Excellence on Tissue Engineering and Regenerative Medicine, University of Minho, AvePark, Zona Industrial da Gandra, 4805-017 Barco, Guimarães, Portugal

⁴ ICVS/3B's-PT Government Associate Laboratory, 4806-909 Braga/Guimarães, Portugal

⁵ Department of Experimental Medicine, University of Salento, c/o Campus Ecotekne, via Monteroni, 73100 Lecce, Italy